

1 This manuscript is a preprint and has been submitted for publication. Subsequent
2 versions may have slightly different content. The DOI of the peer reviewed publication
3 will be provided if accepted. Please contact the authors if you have any questions or com-
4 ments on this manuscript.

Towards Robust River Plastic Detection: Combining Lab and Field-based Hyperspectral Imagery

Paolo Tasseron¹, Louise Schreyers¹, Joseph Peller², Lauren Biermann³, Tim
van Emmerik¹

¹Hydrology and Quantitative Water Management Group, Wageningen University and Research, 6708 PB
Wageningen, The Netherlands

²Plant Sciences Group, Wageningen University and Research, 6708 PB Wageningen, The Netherlands

³Plymouth Marine Laboratory, Prospect Place, Plymouth PL1 3DH, UK

Key Points:

- Lab-based hyperspectral imagery used in classifier algorithms can detect plastics in natural environments with accuracies up to 93.6%.
- Spectral Angle Mapper (SAM) algorithms are most robust for plastic pixel detection in challenging dynamic environmental conditions.
- The hyperspectral dataset we present can be used on multiple scales, supporting the design of new equipment and future satellite missions.

Corresponding author: Paolo Tasseron, paolo.tasseron@wur.nl

Abstract

Plastic pollution in aquatic ecosystems has increased dramatically in the last five decades, with strong impacts on human and aquatic life. Recent studies endorse the need for innovative approaches to monitor the presence, abundance, and types of plastic in these ecosystems. One approach gaining rapid traction is the use of multi- and hyperspectral cameras. However, most experiments using this approach were in controlled environments, making findings challenging to apply in natural environments. We present a method linking lab- and field-based identification of macroplastics using hyperspectral data (1150-1675 nm). Experiments using riverbank-harvested macroplastics were set up in a laboratory environment, and on the banks of the Rhine River. Representative pixel selections of eleven lab-based images ($n = 786,264$ pixels) and two field-based images ($n = 40,289$ pixels) were used to analyse the differences between these environments. Next, classifier algorithms such as support vector machines (SVM), spectral angle mappers (SAM) and spectral information divergence (SID) were applied, because of their robustness to varying light conditions and high accuracies in mapping spectral similarities. Our results showed that SAM classifiers are most robust in separating plastic pixels from background elements. By applying lab-based data for plastic detection in field-based images, user accuracies for plastics to up to 93.6% ($n = 8,370$ plastic pixels) were attained. This study provides key fundamental insights in linking lab-based data to plastic detection in the field. With this paper we aim to contribute to the development of future spectral missions to detect and monitor plastic pollution in aquatic ecosystems.

1 Introduction

Plastic pollution in aquatic ecosystems has increased drastically in the last decades, with strong impacts on human and aquatic life. Recent estimates suggest 19-23 million metric tonnes of macroplastic enter aquatic ecosystems, of which 0.8-2.7 million metric tonnes enters the oceans through rivers annually (Borrelle et al., 2020; Meijer et al., 2021). Therefore, there is a need for innovative approaches to monitor the presence and abundance of plastics in aquatic ecosystems (Maximenko et al., 2016; van Emmerik et al., 2018). An approach gaining rapid attention in the remote sensing community is multispectral or hyperspectral imaging of plastics. Hyperspectral imaging of plastics is key to better understand plastic-specific detection features and the subsequent design of new monitoring instruments (Tasseron et al., 2021; Garaba et al., 2020). Subsequently, these tech-

52 niques offer potential for upscaling and harmonization plastic monitoring across aquatic
53 ecosystems.

54 Recent studies have shown plastics are characterised by unique spectral reflectance
55 signatures in the near infrared (NIR) to shortwave infrared (SWIR) part of the electro-
56 magnetic spectrum, especially in the 1100 – 1700 nm range. Most of the studies focused
57 on characterising the reflection signatures in controlled environments of virgin plastics
58 (Tasseront et al., 2021; Mehrubeoglu et al., 2020; Bonifazi et al., 2018; Moroni et al., 2015;
59 Moroni & Mei, 2020), marine or riverbank-harvested plastics (Goddijn-Murphy & Du-
60 faur, 2018; Karlsson et al., 2016; Corbari et al., 2020), or a combination of virgin plas-
61 tics and harvested plastics (Garaba et al., 2021; Garaba & Dierssen, 2020; Knaeps et al.,
62 2021; Serranti et al., 2018; Moshtaghi et al., 2021). Only few experiments with hyper-
63 spectral imaging systems to detect macroplastics have been performed in aquatic envi-
64 ronments (Garaba et al., 2018; Balsi et al., 2021; Cocking et al., 2022).

65 Therefore, it is imperative to understand how laboratory experiments or experi-
66 ments in controlled environments relate to measurements in natural aquatic ecosystems.
67 As the number of multispectral and hyperspectral reference databases and libraries is
68 increasing (e.g. (Tasseront et al., 2021; Garaba & Dierssen, 2020; Knaeps et al., 2021)),
69 the potential for their usage in identification and detection of plastics in aquatic ecosys-
70 tems is growing. Goddijn-Murphy and Dufaur (2018) evaluated plastic identification al-
71 gorithms for a field experiment and laboratory measurements. They concluded many fac-
72 tors such as the plastic polymer composition, transparency, shape, surface roughness and
73 lighting conditions to affect the correlation between reflectance patterns in the field and
74 laboratory experiments. In addition, Martínez-Vicente et al. (2019) argued it is a chal-
75 lenge to confirm to what extent reflection characteristics observed in a laboratory can
76 be used for detecting floating macroplastics in aquatic ecosystems.

77 It is currently unclear to what extent hyperspectral imaging of plastics in controlled
78 environments is useful for detecting and identifying floating plastics in rivers and on river-
79 banks. Yet, the potential of multispectral and hyperspectral imaging for plastic detec-
80 tion is high (Goddijn-Murphy & Dufaur, 2018; Balsi et al., 2021; Huang et al., 2021).
81 Therefore, this study develops insights in linking lab- and field-based hyperspectral meth-
82 ods for identification of macroplastics. First, an assessment of the reflectance patterns
83 in natural aquatic ecosystems is made to understand how plastic signatures behave in

84 these environments. Second, a direct comparison with reflectance of plastics in a con-
85 trolled is made to assess the differences and how these can be managed in a classifier.
86 Lastly, an indication of the accuracy for using lab-data to classify field images is given,
87 to enhance the potential of former lab-studies for future field detection and monitoring
88 of macroplastics. With this paper, we aim to bridge the gap between experiments in con-
89 trolled and natural environments. The usage of existing lab- data and methods for nat-
90 ural environments could accelerate the harmonization of plastic monitoring in polluted
91 aquatic environments.

92 **2 Methods**

93 **2.1 Riverbank-harvested plastic samples**

94 In this study, riverbank macrolitter was harvested from two different locations for
95 the hyperspectral imaging in both environments. For the controlled environment, the
96 items were harvested from the north Riverbank of the Rhine River near Rhenen ($51^{\circ}57'12.6''$ N
97 $5^{\circ}34'31.5''$ E), in a 100 meter (parallel to river) by 25 meter sampling area. These items
98 were collected as part of the riverbank litter monitoring programme “Clean Rivers” (Reinders
99 & Land-Zandstra, n.d.). After categorisation based on the River-OSPAR protocol as ap-
100 plied in van Lieshout et al. (2020), all litter items were scanned floating in water using
101 a VIS-SWIR (400-1700 nm) double-camera setup as described in Tasserone et al. (2021).
102 For this study, only the NIR-SWIR range (1150 – 1675 nm) was used for all analyses.
103 In total, 78 items were scanned, consisting of 58 plastic items and 13 aluminium items
104 (Fig. 1a-d). The remaining eight items are a miscellaneous collection of paper, rubber
105 and glass which were not used in subsequent analyses.

106 For the hyperspectral imaging in a natural aquatic environment, plastic litter items
107 harvested in a 100 meter by 5 meter area from the Meuse riverbank near Griendpark,
108 Maastricht ($50^{\circ}51'15.5''$ N $5^{\circ}41'50.0''$ E) were used. These items were collected as part of
109 a floating macroplastic monitoring programme “Pilot monitoring floating litter and macroplas-
110 tics in the Dutch Rhine and Meuse rivers” (van Emmerik & de Lange, 2022). In total,
111 26 plastic items were arranged in a wooden frame (Fig. 1e). This collection consists of
112 a variety of hard plastics (high-density polyethylene (HDPE), polypropylene (PP)), soft
113 plastics (low-density polyethylene (LDPE)), foams (polystyrene (PS), expanded polystyrene
114 (E-PS)) and polyethylene terephthalate (PET) bottles. The diverse colours of the items



Figure 1. Riverbank-harvested items from Rhenen used for hyperspectral imaging in controlled environment (a-d); frame with riverbank-harvested items from Maastricht used for hyperspectral imaging in natural environment (e).

115 helps to understand how darker coloured items are reflecting light differently from lighter
 116 coloured items.

117 **2.2 Experimental setups - controlled environment and natural environ-** 118 **ment**

119 The hyperspectral imaging in this study was all conducted in the near-infrared (NIR)
 120 to shortwave infrared (SWIR) part of the electromagnetic spectrum, spanning from 1150
 121 to 1675 nm. Different cameras were used for both environments, as described in the next
 122 sections.

123 **2.2.1 Controlled lab environment**

124 The hyperspectral imaging of the riverbank-harvested litter in the controlled en-
125 vironment was performed using the Specim FX17 camera (Konica Minolta Company,
126 Oulu, Finland). This line-scanning camera covers the electromagnetic spectrum between
127 900-1700 nm in 112 spectral bands. All technical information regarding the integration
128 time, resolution and effective pixel size of this camera as well as the illumination and rel-
129 ative reflectance conversion is summarised in Tasserou et al. (2021). Fig. 2a shows the
130 experimental setup used in Tasserou et al. (2021). The imaging of the riverbank litter
131 was performed prior to this study. The raw image data was unexplored by these authors
132 and was downloaded online for further analysis in this study. Only the data from the Specim
133 FX17 camera was used, since the spectral range of the Specim FX10 camera as shown
134 in Fig. 2a is outside the scope of this study.

135 **2.2.2 Natural aquatic environment**

136 Hyperspectral images were taken in a natural environment using the sample items
137 depicted in Fig. 1e and the setup shown in Fig. 2b. We used the Snapscan SWIR hy-
138 perspectral imaging camera (IMEC, Leuven, Belgium) which covers the electromagnetic
139 spectrum from 1150 to 1675 nm in 100 equally spaced spectral bands. It captures with
140 an integration time ranging from 20ms – 65ms, depending on acquisition parameters, light-
141 ing, and the reflectance characteristics of the objects. The camera has a maximum spa-
142 tial resolution of 1200 x 640 pixels, although a smaller resolution of 520 x 640 pixels was
143 used for this study. As opposed to the Specim FX17, the Snapscan SWIR camera has
144 an integrated line scan sensor which allows using a tripod for scanning the samples.

145 The hyperspectral images were taken on a groyne of the Waal River, near Ochten,
146 the Netherlands (N 51°54'13.3" E 5°33'52.7"). This location was chosen because it is char-
147 acterised by diverse background elements such as sand, rocks, gravel, and various types
148 of vegetation which are the main components composing Dutch riverbanks (De Graaf
149 et al., 1990). Moreover, the ability to park a car in close vicinity of the river allowed pow-
150 ering the camera with the car's battery without the need of expensive deep-cycle bat-
151 teries.

152 On the 28th of May 2021, hyperspectral data was acquired in a cloud-free setting
153 between 11:07 and 12:19. During the experiment, the solar altitude angle ranged from

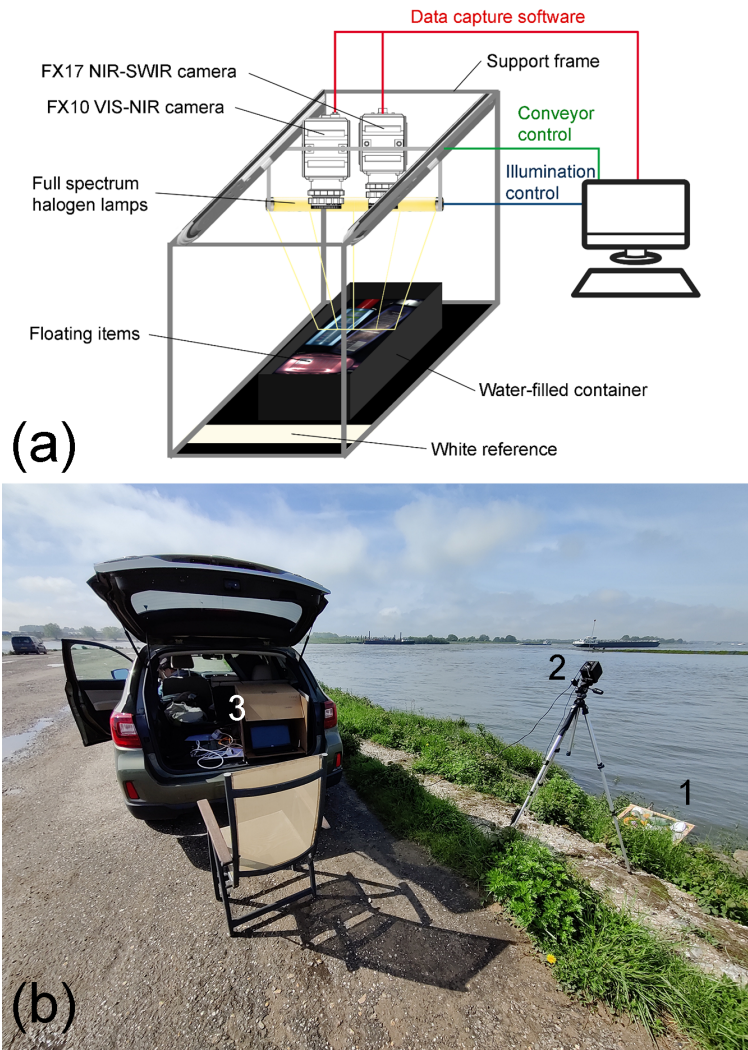


Figure 2. Hyperspectral imaging setup used by Tasseron et al. (2021) (a); Hyperspectral imaging setup in the natural environment (b) with riverbank-harvested sample items (1), IMEC Snapscan SWIR hyperspectral camera (2), laptop with data capture software and power source (3).

154 48.35° – 56.26°, and the azimuth from 122.61° – 146.95°, illuminating the samples from
 155 the south-east. In order to account for these changing conditions, the camera’s white ref-
 156 erence was recalibrated every five minutes by using a white sheet of optical grade Spec-
 157 tralalon, similar to the white reference used in Tasseron et al. (2021). Images were shot
 158 with various integration times, to ensure optimal exposure of both light and dark-coloured
 159 sample items.

2.3 Data preparation and ROI selection

To allow the comparison of the spectral signatures between the two environments, several data pre-processing steps had to be undertaken. First, the hyperspectral data of the controlled environment underwent manual reflectance correction (1) and intensity normalisation (2) prior any subsequent analysis (Tasserou et al., 2021). An overview of the constituents of these equations is found in Appendix A (Table 1). For the hyperspectral imagery in the natural environment, the reflectance correction and intensity normalisation were executed directly by the data capturing software using the same equations. The reflectance correction was done using averaged reflectance values per wavelength

$$R_n = (R_0 - R_B)/(R_W - R_B) \quad (1)$$

$$R_{ni} = (R_n - \min(R_n))/(\max(R_n) - \min(R_n)) \quad (2)$$

Next, regions of interest (ROIs) were manually annotated on the imagery data of both environments, using the PerClass Mira toolbox in MATLAB. Similar to Tasserou et al. (2021), a paintbrush tool was used to define each ROI according to a distinct class. For the lab environment, three classes were established, with a group of pixels being either: (1) water, (2) vegetation or (3) plastic. A total of 786,264 pixels were annotated. For the data captured at the Waal River, the ROIs were assigned one of the following six classes: (1) water, (2) vegetation, (3) wood, (4) rock, (5) plastic, and (6) sand. For each of these classes in both environments, the average spectral signatures were calculated. A pixel-based approach was chosen instead of an object-based image analysis (OBIA), because of the restrictions in resolution when extrapolating the methods to airborne- or space borne imagery. In remote sensing studies using satellite imagery (e.g. (Biermann et al., 2020; Themistocleous et al., 2020)), there are only few (mixed) pixels available, which discourages the use of OBIA. An overview of the ROI selection of the data captured in the natural environment is shown in Fig. 3.

Since the spectral range and resolution varied for both cameras, three manipulations were done on the data acquired in the lab. First, the range of the average spectral signatures was matched by discarding the data outside the 1150 – 1675 nm range. Second, the remaining 74 hyperspectral bands were linearly interpolated to match the 100 bands of the Snapscan SWIR camera. Third, a manual selection of the Snapscan SWIR

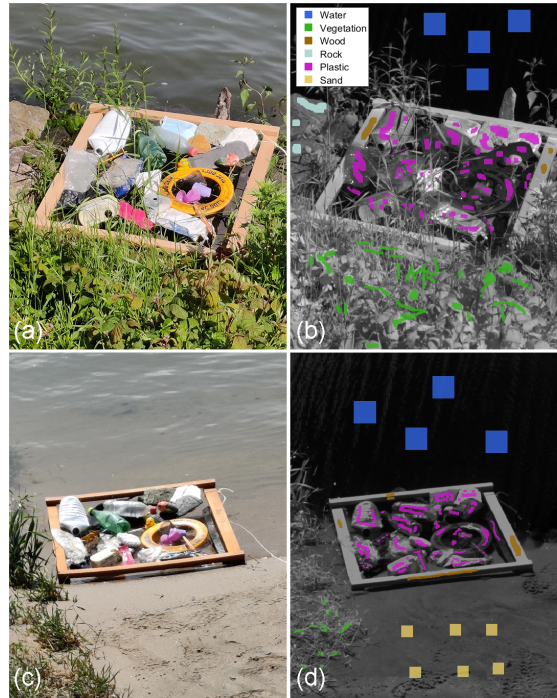


Figure 3. Annotated ROIs on the two images constituting the natural environment pixel dataset used for further analysis (b,d) and their respective RGB-images (a,c). The ROIs in b and d consist of 23.804 and 16.485 pixels, respectively.

190 bands that were closest to the Specim FX17 bands resulted in an imagery dataset of both
 191 cameras with 74 hyperspectral bands. More advanced and scientifically robust techniques
 192 for matching hyperspectral ranges exist (e.g., (Ren et al., 2020; Al-Khafaji et al., 2017))
 193 but are outside the scope of this study. All three manipulations are done in MATLAB.

194 **2.4 Support Vector Machine (SVM) and Spectral Angle mapper (SAM)** 195 **classifiers**

196 Two types of classifiers are applied on the dataset to understand their applicabil-
 197 ity in linking laboratory experiments and field observations. First, a support vector ma-
 198 chine algorithm is used with training data from both lab- and field observations using
 199 the perClass toolbox in MATLAB. The main advantages of support vector machines is
 200 their robustness to noisy and complex input data (Kumar et al., 2015), the small num-
 201 ber of training samples needed (Gopinath et al., 2020) and the ability to efficiently han-
 202 dle high dimensional hyperspectral datasets (Van Belle et al., 2011). Main drawbacks

of SVMs include the time-consuming process of selecting a suitable kernel function and model training, especially with larger datasets (Deka, 2014), the lack of a probabilistic explanation for the classification, and a higher risk of overfitting (Chen et al., 2017). Overfitting occurs when an algorithm or model works well on a training dataset, but performs poorly on testing datasets (Ying, 2019).

Next, the Spectral Angle Mapper (SAM) algorithm, Spectral Information Divergence (SID) and a logarithmic combination of the two (SID-SAM) algorithms from the hyperspectral Image Processing Toolbox™ are tested. A detailed explanation of how these algorithms work is found in appendix C. These algorithms have several advantages in comparison with SVM-based classifiers. For instance, they are almost insensitive to differences in the intensity values of a signal (Petropoulos et al., 2010). In addition, SAM classifiers are easy and accurate methods for mapping the spectral similarity of a given pixel to a reference spectrum or a set of reference spectra (Girouard et al., 2004). One main disadvantage of SAM classifiers is that every pixel is labelled based on the closest reference spectrum, implying a pixel that does not belong to any of the predefined categories is classified incorrectly. This can easily be resolved by setting boundaries beyond which pixels should not be classified. To demonstrate the influence of narrowing the decision boundaries, the SAM-classifier is computed using three decision boundary angles of 7.5°, 10° and 15°. Another disadvantage is that these classifiers do not consider mixed pixels and sub-pixel values (Girouard et al., 2004), yet this is not an issue with the resolution and quality of the hyperspectral data used in this study but can be problematic using satellite or UAV images.

A flowchart describing the steps taken in the classification procedure is summarised in Figure 16 (Appendix C).

3 Results and discussion

First, it is established which reflectance patterns characterise riverbank-harvested litter in a controlled environment. A similar procedure is followed for macroplastics in aquatic ecosystems and a comparison between the two environments is made. Second, the accuracy of the SVM, SAM, SID, and SID-SAM classifier algorithms in the identification of plastics in both environments is established. The SID and SID-SAM algorithms showed significantly lower classification accuracies than the SAM algorithm.

234 **3.1 Reflectance patterns of water, vegetation, and plastics in various en-**
 235 **vironments**

236 Fig. 4 shows the average reflectance signatures of water, vegetation and plastic in
 237 lab and field-based experiments from 1150 – 1675 nm. Clearly, multiple differences are
 238 present between the lab and field-based signatures in all three classes.

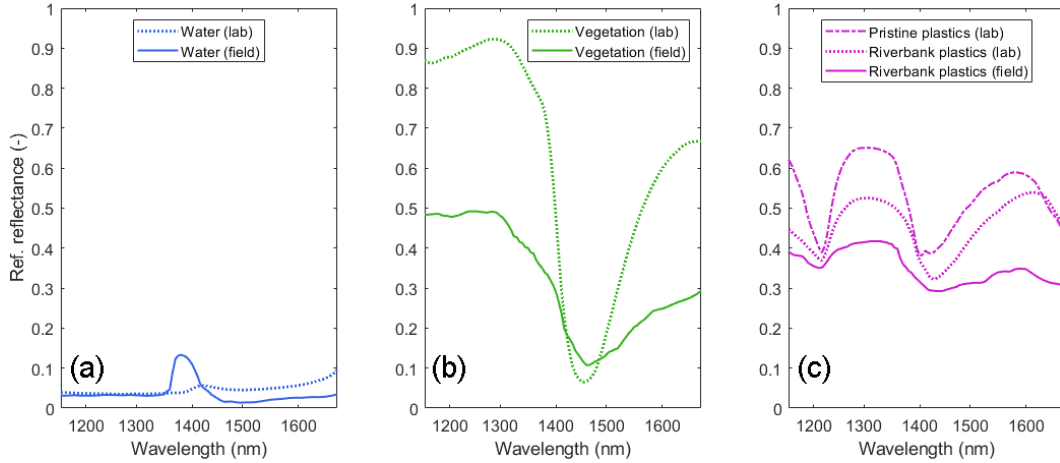


Figure 4. Lab and field-based reflectance signatures of: (a) water, (b) vegetation, and (c) plastic. Dotted lines indicate signatures as measured in the controlled environment. The ‘dash-dot’ line in (c) is the average spectral signature of pristine plastics as determined by Tasserou et al. (2021), which is used just for a frame of reference.

239 First, the spectral signature of water has similar intensities over the entire hyper-
 240 spectral range, with one exception. A slight reflectance peak is apparent in the water
 241 reflectance measured in the field between approximately 1370 and 1430 nm. This arti-
 242 ficial peak was caused by a relative low signal-to-noise ratio of the hyperspectral imag-
 243 ing sensor outdoors. When comparing the range of this peak with the spectral energy
 244 curve of solar radiation, a strong absorption window of H_2O molecules is present (Lacis
 245 & Hansen, 1974). In fact, the transmittance of the atmosphere is almost zero at the wave-
 246 length where the water reflectance in Fig. 4a peaks (Hottel, 1976). Even though the use
 247 of a white reference cancels out differences in atmospheric transmittance, the large amount
 248 of noise caused by the extremely low transmittance is most likely the cause of this ap-
 249 parent peak in the spectral signature.

250 Comparing the two spectral signatures of vegetation, an important dissimilarity
251 between the signatures is a large difference in the intensity. A likely reason for this dis-
252 similarity is the difference in integration time of the sensors and illumination intensity
253 of the samples in both environments. Additionally, the leaf water content significantly
254 influences the strength of the absorption peak at 1450 nm (Danson et al., 1992), which
255 could be different for both environments. The overall shape of both signature is relatively
256 similar, having a high reflection between 1150 – 1300 nm, an absorption peak around 1450
257 nm and a steady increase in reflection between 1450 – 1675 nm. As mentioned earlier,
258 SVM-based classifiers are more sensitive to differences in intensity than SAM classifiers.
259 The latter could result in a more robust and accurate classification for SAM classifiers
260 in comparison with SVM-based classifiers. Third, the spectral signatures of plastics are
261 shown in Fig. 4c. Like vegetation, the overall shape with absorption and reflection peaks
262 is comparable between the three different signatures. Key differences between the lab-
263 based and field-based spectral signatures of riverbank-harvested plastics is the intensity
264 and strength of the absorption peaks. With controlled and stable light conditions, the
265 average lab-based signature is relatively smooth with a range of approximately 0.37 –
266 0.52 in intensity. In contrast, the average field-based signature is less smooth and has
267 a smaller intensity range, in which the absorption peaks are slightly less pronounced. Tasseron
268 et al. (2021) emphasised the importance of the absorption peaks in distinguishing plas-
269 tics from vegetation and water. Luckily, the atmospheric absorption of H_2O molecules
270 is not in overlapping with the wavelengths of the absorption peaks of plastics, which sub-
271 dues the influence of sunlight in the classification of plastics. Different types of plastic
272 have different reflection signatures (Zheng et al., 2018), which would imply a larger intra-
273 class variability when averaging the signature for all plastic types. Nevertheless, the av-
274 erage signature from plastics is characterised by a high inter-class variability compared
275 to water and vegetation, thus not strongly influencing the classifier algorithms.

276 **3.2 Classifier algorithms for identification of plastics in both environ-** 277 **ments**

278 ***3.2.1 Support Vector Machine pipelines***

279 A distinctive property of the SVM pipelines is to separate between the six differ-
280 ent classes of the ROIs used for training, which each have a unique spectral signature.
281 Fig. 5 shows two classified images using the ‘pipeline_svm’ (trained using ROIs from Fig.

282 2b) and ‘pipeline_svm_field’ (trained using ROIs from Fig. 2d) pipelines. It is evident
 283 that the RBF kernel used in these pipelines performs well when using ROIs from the same
 284 image yet is not very robust when using a training dataset based on a different image.
 285 This emphasizes the high risk of overfitting with SVM classifiers. In fact, the confusion
 286 matrix in Fig. 9a (Appendix B) shows that the user’s accuracy of the plastic class is only
 287 30.1%. Most pixels that should have been classified as plastic, are classified as sand and
 288 vegetation instead. In addition, a large share of the pixels that should have been clas-
 289 sified as water are classified as plastics. This is not reflected that in the confusion ma-
 290 trix in Fig. 9b (Appendix B), as it states 93.8% of water pixels are classified correctly.
 291 The latter is caused by the chosen ROIs for computation of the confusion matrix. As seen
 292 in Fig. 3b, the annotated ROIs for water mostly cover the pixels that were classified cor-
 293 rectly.

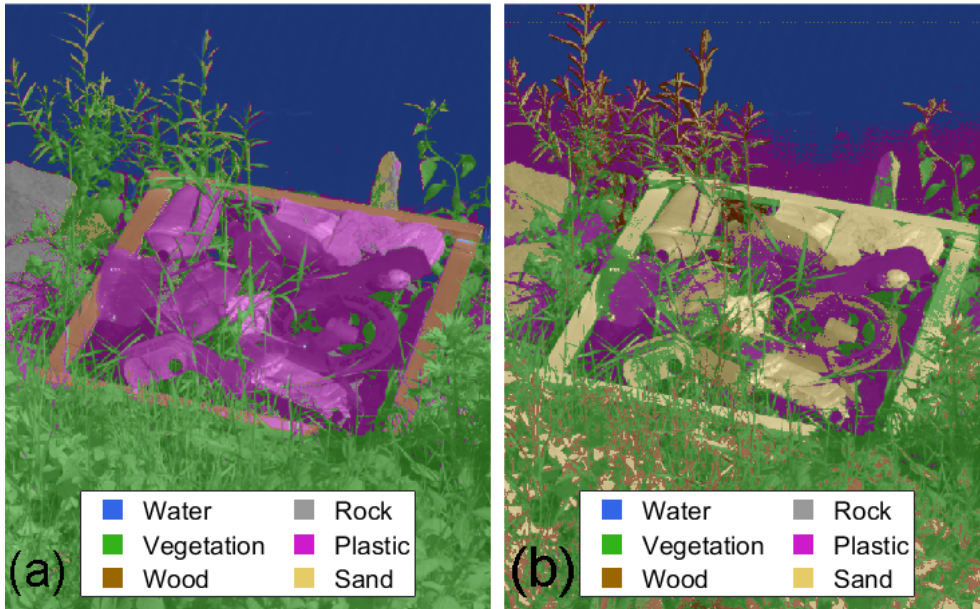


Figure 5. Support Vector Machine classified images using: (a) ROIs of the same image to classify the entire image, and (b) ROIs of Fig. 2d - different image - used for training the classifier. Associated confusion matrices are found in Fig. 10 (Appendix B).

294 When using the pipelines including lab data for training, the classification is sig-
 295 nificantly different. Fig. 6 shows the classified images using a combination of lab and field
 296 data, and only field data. Clearly, the classification of plastic pixels using lab data in com-
 297 bination with field data for background elements yields poor results. As depicted in Fig.

298 6a, nearly all plastic pixels are not classified at all or classified incorrectly, with a user's
 299 accuracy of 4.3% (Appendix B, Fig. 10). This extremely low accuracy is likely caused
 300 by the difference in signatures derived from lab-data and field-data.

301 Classification accuracies of plastics significantly improve when using only laboratory-
 302 based data, as depicted in Fig. 6b, 6c. The difference between these two classifications
 303 clearly demonstrate a weakness of SVM-classifiers, specifically its sensitivity to changes
 304 in intensity. The intensity of the average lab-based vegetation spectrum is much higher
 305 than the spectrum based on field data. Therefore, the SVM-classifier decided the veg-
 306 etation pixels in Fig. 6b better resemble the plastic spectrum based on intensity, which
 307 resulted in a complete misclassification of vegetation. Halving the intensity values of the
 308 vegetation pixels used for training results in a slightly better classification (Fig. 6c). Yet,
 309 the producer's accuracy of plastic pixels is still only 68.2% (Appendix B – Fig. 10), which
 310 substantiates the dependence on intensity in SVM-based classifiers.

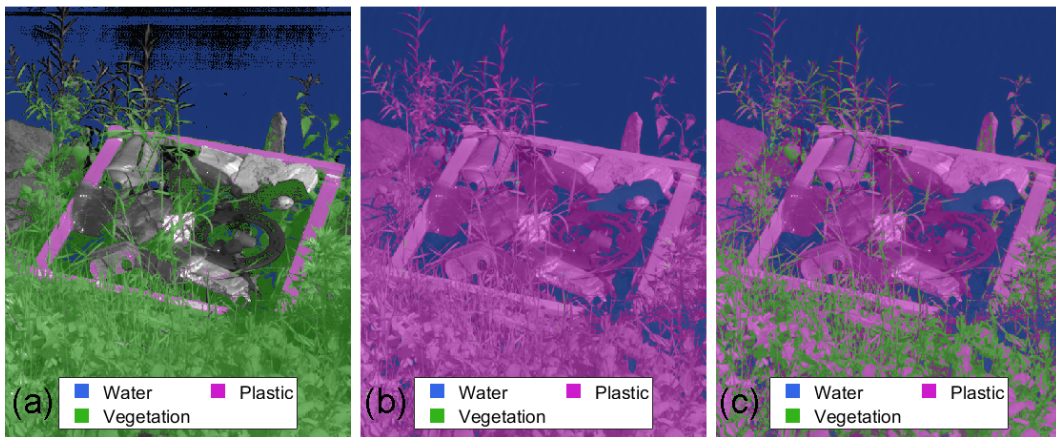


Figure 6. Classified images using support vector machine pipelines with (a) lab data for plas-
 tics, field data for vegetation and water, (b) lab data for all categories, and (c) lab data for all
 categories, with halved intensity of the vegetation pixels.

311 3.2.2 SAM, SID and SIDSAM

312 This section illustrates and quantifies the differences between SAM, SID and SID-
 313 SAM classifications. First, by using field-data to train the algorithms, followed by us-
 314 ing lab-data for training. Lastly, the effect of narrowing the cone of uncertainty of SAM-
 315 based classifications is illustrated. Fig. 7a-c depict the classification results of using these

316 three algorithms trained with field-data. It is clear the SAM algorithm performs best,
 317 with a user's accuracy of 93.5% for plastics (Appendix B – Fig. 11), as opposed to 18.2%
 318 and 68.6% for SID and SIDSAM, respectively. However, the rock in the image is clas-
 319 sified as plastic when using SAM, whereas it is classified as sand using the other two al-
 320 gorithms (Fig. 7a-c). Even though the rock is classified incorrectly, the producer's ac-
 321 curacy is higher for SID and SIDSAM (99.5% and 99.2%, respectively) than for SAM
 322 (85.8%).

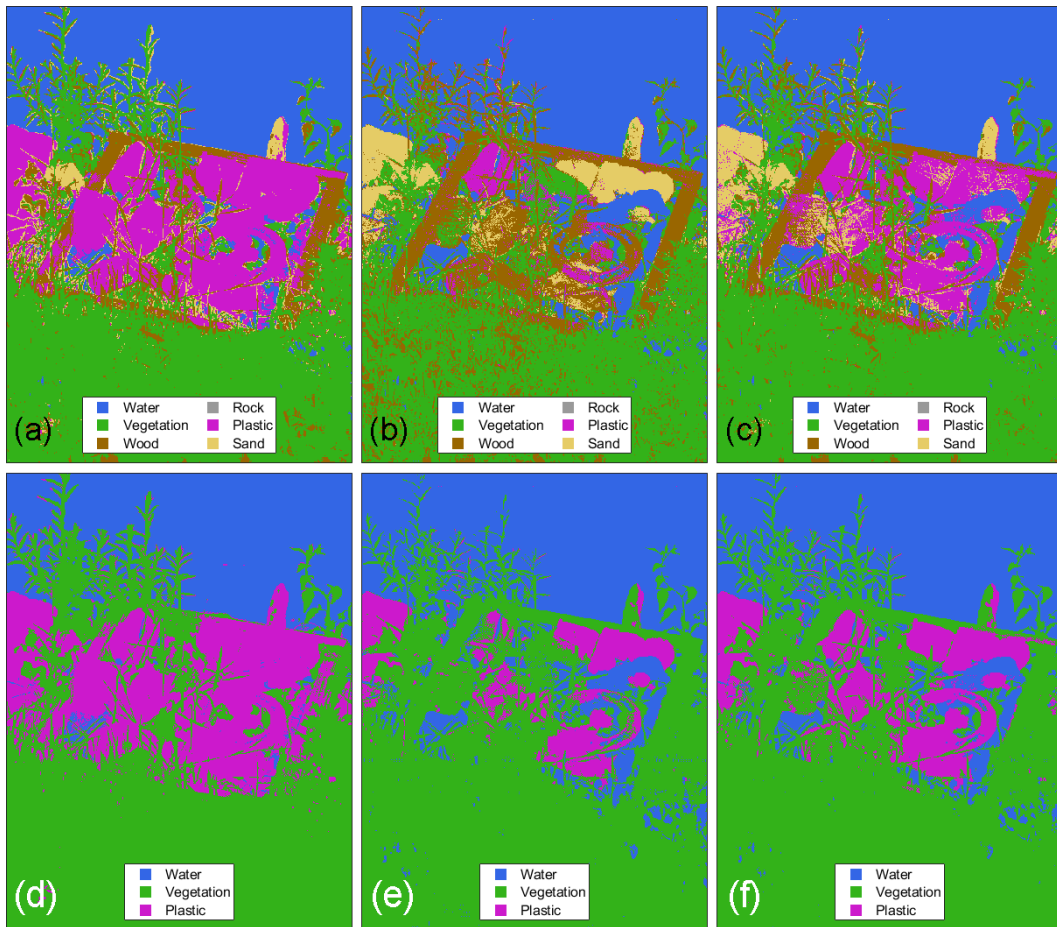


Figure 7. Classifications with training dataset based on ROIs of Fig. 3d, using (a) SAM, (b) SID, (c) SIDSAM, and and Classifications with training dataset based on lab-data, using (d) SAM, (e) SID, (f) SIDSAM

323 The SID algorithm, using a probabilistic approach based on intensity, misclassi-
 324 fies most plastic pixels with a low intensity. For example, the plastic bottle in the top
 325 left of the Frame (Fig. 7b) seems to be the only cluster of pixels recognised as plastic

326 by this algorithm. Referring to Fig. 1e, this bottle (id 1) is opaque and white, which means
 327 it has a significantly higher reflection value than all the other plastic items. Therefore,
 328 it is likely the low user’s accuracy for plastics of this algorithm is caused by higher in-
 329 tensities in the training dataset. In fact, the black foam (Fig. 1e – id 9) is classified as
 330 water both for SID and SAM. This misclassification makes sense when considering the
 331 probabilistic nature of intensities. Since darker coloured items have lower reflectance in-
 332 tensities, the darker plastic items are more likely to resemble the spectra of wood, sand,
 333 vegetation or even water. From Fig. 7c, it is clear this effect is smaller when using SID-
 334 SAM, but still yields a smaller user’s accuracy for plastic pixels.

335 Next, when using only lab data for classification, similar patterns between the three
 336 algorithms are found, as depicted in Fig. 7d-f. A user’s accuracy for plastics of 93.6%,
 337 50.2% and 65.4% is reached for SAM, SID and SIDSAM, respectively (Appendix B – Fig.
 338 12). The producer’s accuracy for plastics is 99.8% for SAM, and 100% for SID and SID-
 339 SAM, indicating that nearly no vegetation or water pixels were classified as plastic. It
 340 is evident the SID and SIDSAM algorithms perform worse when classifying pixels with
 341 a low reflectance intensity. In fact, darker coloured items are misclassified in a similar
 342 fashion when compared with the algorithms trained with field-data.

343 **3.2.3 SAM with various decision boundaries**

344 This section illustrates the influence of different decision boundaries at 7.5°, 10° and
 345 15° using SAM, Fig. 8a-c shows the classification results using field data as a training
 346 dataset. As illustrated in Fig. 13 (Appendix B), an advantage of narrowing the cone is
 347 that both the user’s and producer’s accuracy of plastics increase. For example, most pix-
 348 els that compose the rock in Fig. 8a are classified as plastic. With a narrower decision
 349 boundary cone, the same rock region in Fig. 8c mainly consists of unclassified pixels.

350 When applying the same decision boundaries on the classifier using lab data as ref-
 351 erence spectra, a few major differences are present (Fig. 8d-f). For example, almost all
 352 vegetation and water pixels become unclassified when using a decision boundary of 7.5°.
 353 For plastics, a cone of 15° leads to approximately 8.0% of plastics being missed, whereas
 354 the cone of 7.5° results in 85.6% of plastic pixels being missed. As elaborated in section
 355 4.1, several differences in the reflection spectra of lab- and field-based imaging are present.
 356 It is likely these differences are large enough to cause most pixels in all categories be-

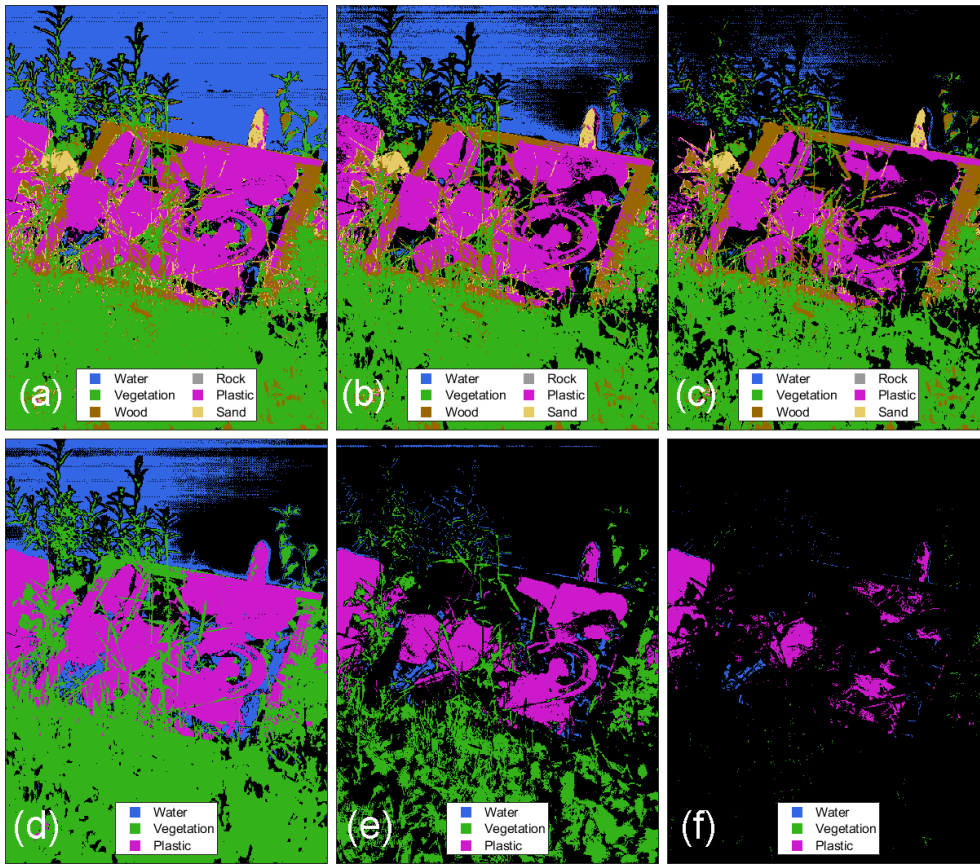


Figure 8. SAM classification using field data with decision boundaries set at (a) 7.5° , (b) 10° and (c) 15° , and classification using lab data with decision boundaries set at (d) 7.5° , (e) 10° and (f) 15° . Black pixels indicate unclassified pixels, that do not fall within the decision boundary region.

357 ing unclassified when using the 7.5° decision boundary. As illustrated in Fig. 14 (Ap-
 358 pendix B), the increase in user's and producer's accuracy is only marginal, which is ren-
 359 dered futile when considering the large share of missed pixels with narrowed decision bound-
 360 aries. Lastly, the rock is still classified as plastic, whereas most pixels that should be clas-
 361 sified as plastic are being missed (85.6%). Therefore, the effect of narrowing the deci-
 362 sion boundary when using lab-data to classify field-data is mainly disadvantageous.

363 However, it is also evident that narrowing the decision boundary results in an in-
 364 creased number of unclassified pixels. In fact, Fig. 15 (Appendix B) shows the percent-
 365 age of unclassified pixels with a narrowing decision boundary region. For the classifica-
 366 tion with field data, a cone of 15° results in a loss of approximately 3.7% of the pixels
 367 that should be classified as plastic. This quickly increases to 42.1% when a cone of 7.5°

368 is used. Therefore, it is necessary to find a balance between the number of missed pix-
369 els and the accuracy of the classification.

370 **4 Synthesis and Outlook**

371 Based on the knowledge that macroplastics reflect light in a unique way compared
372 to other floating litter and natural or anthropogenic background materials (Tasserou et
373 al., 2021; Garaba et al., 2020; Mehrubeoglu et al., 2020; Bonifazi et al., 2018; Moroni et
374 al., 2015; Moroni & Mei, 2020; Goddijn-Murphy & Dufaur, 2018; Karlsson et al., 2016;
375 Corbari et al., 2020; Garaba et al., 2021; Garaba & Dierssen, 2020; Knaeps et al., 2021;
376 Serranti et al., 2018; Moshtaghi et al., 2021; Garaba et al., 2018), this study addressed
377 two objectives. First, an understanding of the difference between lab-based and field-
378 based hyperspectral imaging was made by comparing the associated hyperspectral sig-
379 natures. The riverbank-harvested plastic samples investigated for this purpose were pre-
380 sumed to be an appropriate subset of commonly found litter along Dutch riverbanks, cor-
381 roborated by van Emmerik et al. (2020). Second, it was investigated how plastics can
382 best be distinguished from background elements and materials by exploiting various clas-
383 sification approaches. In doing so, a foundation for using laboratory data to train mod-
384 els that classify field-images was successfully made.

385 The results strongly suggest lab-based data can be used in a spectral angle map-
386 per (SAM) algorithm to classify hyperspectral images taken in the field. Previous stud-
387 ies indicated SAM is relatively robust to changes in illumination intensity and mapping
388 spectral similarities compared to other classification methods (Petropoulos et al., 2010;
389 Girouard et al., 2004; Murphy et al., 2012). Therefore, the detection of plastic pixels was
390 still successful even though the environmental factors are highly different from lab con-
391 ditions. The large number of annotated pixels from the lab-based images ($n = 786,264$)
392 allowed the establishment of representative hyperspectral signatures of plastics. Addi-
393 tionally, a high-resolution field image ($n = 332,800$ pixels) allowed thorough analyses of
394 different classification techniques. As a result, the fundamental method resulted in ac-
395 curacies of up to 93.6% for plastics when classifying an image captured at the riverbank.
396 In doing so, our results are amongst the first to tackle the challenge of using lab-based
397 data for field-classification of plastics, which was emphasised by Martínez-Vicente et al.
398 (2019).

399 Yet, one of the main challenges for future hyperspectral field detection of plastics
400 includes the dynamic nature of meteorological conditions (Stuart et al., 2019; Adão et
401 al., 2017), which can significantly affect the image capturing process. In fact, the long
402 integration time of up to 10 seconds per capture required the samples to be completely
403 stationary. Additionally, rapidly changing light conditions such as shadows casted on the
404 objects by clouds required continuous sensor recalibration. Thirdly, extremely low at-
405 mospheric transmittance between 1350 – 1400 nm causes excessive noise in this region
406 of the spectrum, which can be amplified in normalisation techniques. Therefore, it is rec-
407 ommended for future studies to omit such wavelength ranges in their analyses. These
408 factors combined are a major complication for fundamental detection and eventually long-
409 term monitoring. In fact, Stuart et al. (2019) argue that even state-of-the-art hyperspec-
410 tral systems are challenging to use in continuous field monitoring, especially in volatile
411 environments which require outer casing of devices to be weatherproofed (Wilkes et al.,
412 2017). Moreover, long term detection and monitoring of floating litter is technologically
413 restricted by the spatial, spectral, and radiometric resolution of existing hyperspectral
414 sensors (Balsi et al., 2021). Yet, the continuous development of (ultra) compact, lightweight
415 and affordable multispectral and hyperspectral imaging systems (e.g. Wilcox et al. (2018))
416 is promising for future monitoring missions.

417 A key step for further practical application of hyperspectral imaging includes the
418 establishment of reliable and high-quality reference libraries. Various open-access libraries
419 with reference hyperspectral signatures already exist. For instance, the ECOSTRESS
420 spectral library consists of over 3000 hyperspectral signatures of manmade materials, soil,
421 water and vegetation (Borsoi et al., 2020). Developed by NASA, this library is widely
422 used in estimating vegetation abundance and classifying mineral surfaces (Li et al., 2021;
423 Cardoso-Fernandes et al., 2020). Including hyperspectral signatures of plastics as found
424 in (Tasseront et al., 2021; Garaba et al., 2020; Mehrubeoglu et al., 2020; Bonifazi et al.,
425 2018; Moroni et al., 2015; Moroni & Mei, 2020; Goddijn-Murphy & Dufaur, 2018; Karls-
426 son et al., 2016; Corbari et al., 2020; Garaba et al., 2021; Garaba & Dierssen, 2020; Knaeps
427 et al., 2021; Serranti et al., 2018; Moshtaghi et al., 2021; Garaba et al., 2018) and this
428 study in such reference libraries is essential. This can either be done as an addition to
429 existing libraries, or by the establishment of a completely new open-access library specif-
430 ically designed for plastics. All hyperspectral data used for the analyses in this study are
431 available online in such a reference library (data availability statement). The signatures

432 included in these libraries would have a high spectral resolution. This implies a smaller
433 range of bands or even multispectral bands can be selected or interpolated, which can
434 in turn be used in comparison with new field measurements. In addition, the continu-
435 ous development of (ultra) compact, lightweight and affordable hyperspectral imaging
436 systems (e.g. (Wilcox et al., 2018)) is promising for future plastic detection and mon-
437 itoring missions.

438 5 Conclusion

439 Hyperspectral imaging systems provide new opportunities for the detection and the
440 identification of macroplastics in natural environments. First, this study explored the
441 differences and similarities between lab-based and field-based hyperspectral signatures
442 of water, plastic, and vegetation. These findings were in turn used to understand the dif-
443 ferences in performance of various classifier algorithms, and which algorithm performs
444 best. A key factor influencing performance of SVM, SID, and SIDSAM classifiers is the
445 reflectance intensity of the hyperspectral signals. On the contrary, SAM is relatively ro-
446 bust concerning the reflectance intensity and performs best out of these four techniques.
447 Future work should explore the influence of the illumination differences in more detail,
448 as well as the role of additional changing environmental conditions and its impacts on
449 hyperspectral monitoring.

450 Second, this study successfully demonstrated the use of laboratory-based hyper-
451 spectral measurements for identification of plastics in a natural aquatic environment. The
452 latter was realised by using various classification algorithms and assess their effective-
453 ness in detecting plastics using confusion matrices. With accuracies of up to 93.6%, the
454 spectral angle mapper (SAM) algorithm was most successful in separating plastic pix-
455 els from natural background elements. Future work exploring the fundamental applica-
456 tions of similar algorithms should include a wider range of imagery captured under var-
457 ious environmental conditions. This is in turn relevant for long-term detection and mon-
458 itoring of plastics using hyperspectral systems.

459 Continuous technological advances in combination with the fundamental findings
460 in this study and similar studies will eventually lead to monitoring of plastic debris in
461 aquatic ecosystems that is more reliable and consistent than visual or manual counting.
462 Yet, there are still some major developments required before this is realised. As soon as

463 harmonised methods to automatically monitor the presence and abundance of plastics
464 exist, targeted action can be taken at the source of the pollution, rather than at the aquatic
465 ecosystems in which the litter would otherwise end up.

466 **Conflict of interest**

467 The authors declare that the research was conducted in the absence of any com-
468 mercial or financial relationships that could be construed as a potential conflict of in-
469 terest.

470 **Author contributions**

471 Conceptualization: PT, Methodology: PT Formal Analysis: PT Investigation: PT,
472 LS JAP Visualization: PT Data curation: PT Writing–original draft: PT Writing–reviewing
473 and editing: all authors Supervision: JAP, LS, TvE Project administration: PT Fund-
474 ing acquisition: TvE

475 **Data availability statement**

- 476 • The raw imagery files captured in the controlled environment are available online
477 at <https://doi.org/10.4121/14518278>.
- 478 • The raw imagery files captured in the natural environment, MATLAB scripts, and
479 associated data are available online at <https://doi.org/10.4121/20343012>.

480 **Acknowledgments**

481 The authors would like to thank Lei Zhang (IMEC/One Planet), who enabled the
482 trips to the field with the hyperspectral camera. Additionally, the authors would like to
483 thank Marco Balsi (“La Sapienza” University of Rome, Italy) for his efforts in provid-
484 ing his expert opinion and reviewing the draft manuscript prior to submission, improv-
485 ing the quality of the work.

486 **Funding**

487 The work of LS was supported by NWO Open Mind grant 18127. This study is part
488 of the Plastic Plants project, supported by the Discovery Element of the European Space
489 Agency’s Basic Activities (ESA contract no. 4000132682/20/NL/GLC)The work of TvE

490 was supported by the 4TU.Federation Plantenna project, and the Veni research program
491 The River Plastic Monitoring Project with project number 18211, which is (partly) funded
492 by the Dutch Research Council (NWO).

Appendix A - Tables**Table 1.** Constituents of the equations and their description.

Constituent	Description
R_n	Corrected relative reflectance imagery (FX17)
R_0	Raw reflectance dataset (FX17)
R_B	Mean dark reference reflectance (FX17)
R_W	Mean white reference reflectance (FX17)
R_{ni}	Normalised intensity dataset (FX17)

Table 2. Constituents of the equations and their description.

SVM Pipeline name	Training data
pipeline_SVM	ROIs Fig. 3b
"_field	ROIs of Fig. 3d (different training – validation dataset)
"_lab	ROIs Fig. 3b (excluding plastics), and Plastics from lab data (R_{ni})
"_onlylab_10k	Random selection of 10.000 pixels from lab data (R_{ni}) vegetation, riverbank-harvested plastics and water
"_onlylab_10k_vegeta- tion_halved	Random selection of 10.000 pixels from lab data (R_{ni}) vegetation, riverbank-harvested plastics and water. Intensity of vegetation multiplied by 0.5.

494 **Appendix B - Figures**

495 The confusion matrices are characterised by two columns of percentages, labelled
 496 'True Class' (user's accuracy) and 'Predicted Class' (producer's accuracy). The blue tinted
 497 values indicate the % correctly classified pixels ('accuracy'), whereas the red tinted val-
 498 ues indicate the % incorrectly classified pixels.

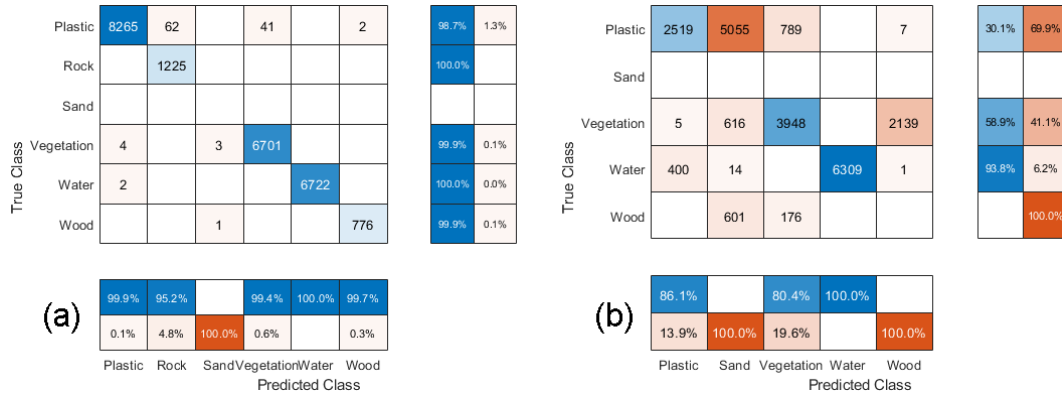


Figure 9. Confusion matrices for SVM-classified image based on (a) ROIs from the same image to classify the entire image, and (b) ROIs of Fig. 2d (Different image) to train the classifier.

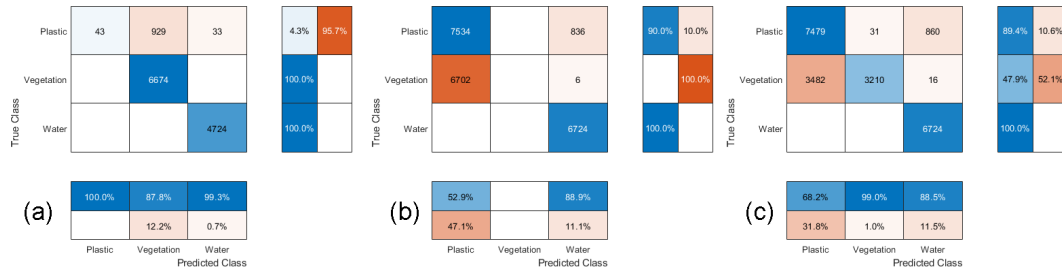


Figure 10. Confusion matrices for SVM-classified image based on (a) lab data for plastics, field data for vegetation and water, (b) lab data for all categories, and (c) lab data for all categories, with the intensity of the vegetation pixels multiplied by 0.5

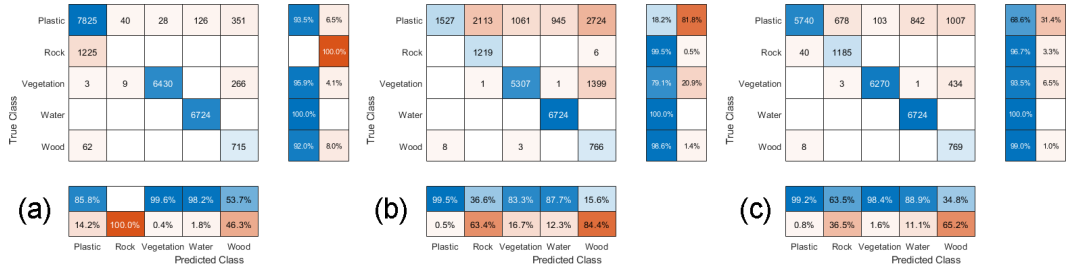


Figure 11. Confusion matrices for: (a) SAM, (b) SID, (c) SIDSAM using field data (ROIs Fig. 3b) for training

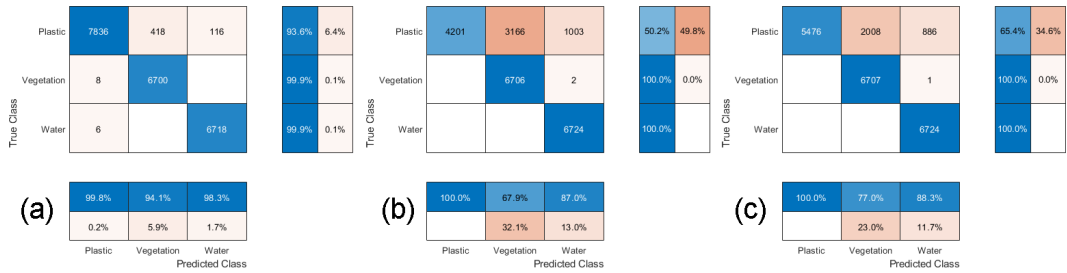


Figure 12. Confusion matrices for: (a) SAM, (b) SID, (c) SIDSAM using lab data for training.

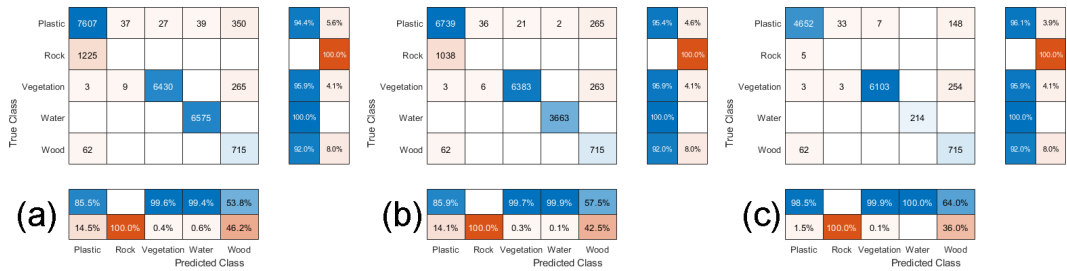


Figure 13. Confusion matrices for SAM-classified image based on field data, with: (a) 15° cone, (b) 10° cone, and (c) 7.5° cone.

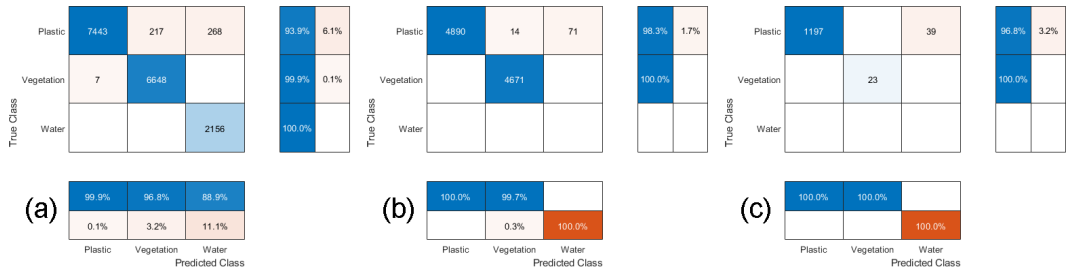


Figure 14. Confusion matrices for SAM-classified image based on lab data, with: (a) 15° cone, (b) 10° cone, and (c) 7.5° cone.

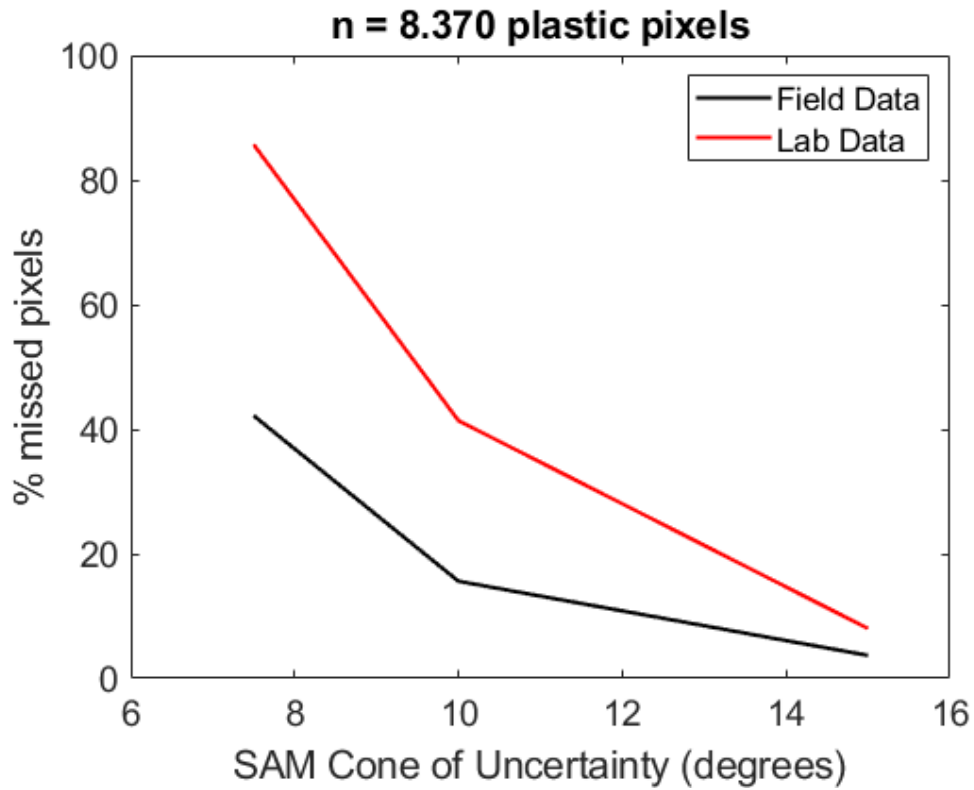


Figure 15. Percentage of missed pixels in classification plotted against the cone of uncertainty (decision boundaries) for field data and lab data.

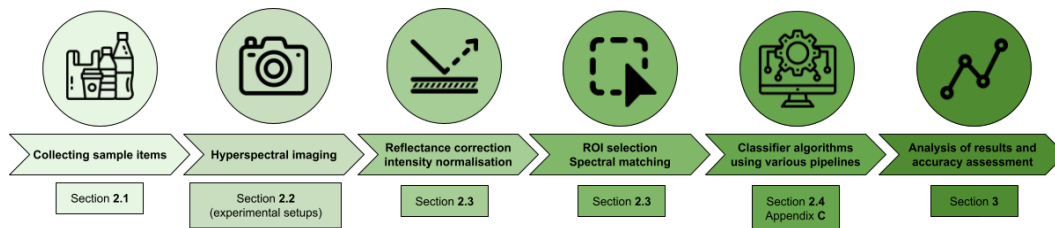


Figure 16. Flowchart describing the classification procedure

499 **Appendix C - Algorithm explanation**

500 **5.1 Support Vector Machine in MATLAB**

501 The support vector machine (SVM) algorithm is used in MATLAB based on lib-
502 SVM (Chang & Lin, 2011). As mentioned earlier, selecting a suitable kernel function for
503 model training is time-consuming, so a default Radial basis function (RBF) kernel is used.
504 An explanation of the mathematics behind this kernel is outside the scope of this study.
505 However, it is important to note the function has two customisable parameters: σ and
506 C . The sigma parameter determines the reach, which defines the importance of points
507 close to the decision boundaries of the classes. A high σ value indicates the decision bound-
508 aries are highly flexed, whereas a low value indicates a more linear decision boundary.
509 Next, the C parameter determines how much misclassification is allowed. Smaller val-
510 ues of C indicate a large margin of error, allowing a substantial number of misclassifi-
511 cations, whereas a high value of C indicates a small margin of error. Like the default RBF
512 function, the default σ and C values are used in classification. Since the SVM algorithm
513 is used for solving a multi-class classification, the default one-against-all strategy is used.
514 This method constructs n_i (number of classes) classifiers in which each classifier sepa-
515 rates class i from all other classes (Liu & Zheng, 2005). These classifiers are then com-
516 bined for a decision which class the pixel spectrum fits best.

517 Several training datasets are used to train five different classification pipelines. An
518 overview of these pipelines is summarised in Appendix A (Table 2). As a baseline ref-
519 erence, the first pipeline is trained using the ROIs as indicated in Fig. 3b to classify the
520 same image used for training. Next, the second pipeline is trained using the ROIs from
521 Fig. 3d, to classify the hyperspectral data belonging to the image in Fig. 3a. This pipeline
522 was trained to assess the influence of using input data from a different field image in SVMs.
523 Thirdly, a pipeline is trained using all ROIs from Fig. 3b, except for plastics. The spec-
524 tral signatures of riverbank-harvested plastics obtained in the lab are used in this pipeline.
525 This pipeline was trained to assess to what extent a combination of using lab and field-
526 based input data is possible. The fourth pipeline is trained using only lab data, with three
527 classes: plastic, vegetation, and water. This pipeline is in line with the main aim of this
528 study, to assess how lab-data can be used for field classification. Lastly, the fifth pipeline
529 is trained using the same data as the fourth pipeline, with the intensity of the vegeta-
530 tion pixels multiplied by 0.5. This is done to emphasise the case that support vector ma-

531 chines are sensitive for changes in intensity values. Confusion matrices are computed for
 532 all pipelines to understand the effect of using different combinations of training datasets
 533 on the accuracy of classification.

534 5.2 SAM, SID, and SID-SAM in MATLAB

535 Spectral angle mapper algorithms measure the spectral similarity between the spectra
 536 of each pixel in the input training dataset, and a specified collection of reference spectra
 537 (Kruse et al., 1993). It is based on the principle of computing the spectral angle distance
 538 between each pixel and the reference spectra in the dataset. The main output of
 539 the SAM algorithm is a vector or matrix with the spectral angle of each pixel relative
 540 to the reference spectra in radians. Low SAM scores indicate strong matches between
 541 the spectrum belonging to the tested pixel and the reference signature. A threshold angle
 542 can be set after which certain pixels should not be classified as the category belonging
 543 to the nearest reference spectrum (Fig. 17). Given the input data t with pixel index
 544 number i and reference spectra R_{ref} of length C , the SAM score α is calculated as:

$$\alpha = \cos^{-1} \frac{\sum_{i=1}^C t_i * R_{ref,i}}{\sum_{i=1}^C t_i^2 * \sum_{i=1}^C R_{ref,i}^2} \quad (3)$$

545 Identical to SAM, the spectral information divergence (SID) algorithm measures
 546 the spectral similarity between the spectrum belonging to a pixel and a collection of reference
 547 spectra or endmember spectra. As opposed to SAM, this method calculates the spectral
 548 similarity based on the divergence between the probability distributions of the tested
 549 pixel and the reference spectra (Chein, 2000). As such, the SID algorithm does
 550 not rely on geometric properties when measuring the discrepancy between the pixel spectra
 551 and reference spectra (Chein, 1999). The main output of the SID algorithm is a vector
 552 or matrix with SID (divergence) scores. Smaller divergence values indicate a pixel
 553 spectrum is more likely to be similar to the reference spectrum (Khaleghi et al., 2014).
 554 Given the input data t with pixel index number i and reference spectra R_{ref} , the distribution
 555 values q_i for the input data are calculated as follows:

$$q_i = \frac{t_i}{\sum_{i=1}^C t_i} \quad (4)$$

556 The distribution values p_i for the reference spectra are calculated as follows:

$$p_i = \frac{R_{ref,i}}{\sum_{i=1}^C R_{ref,i}} \quad (5)$$

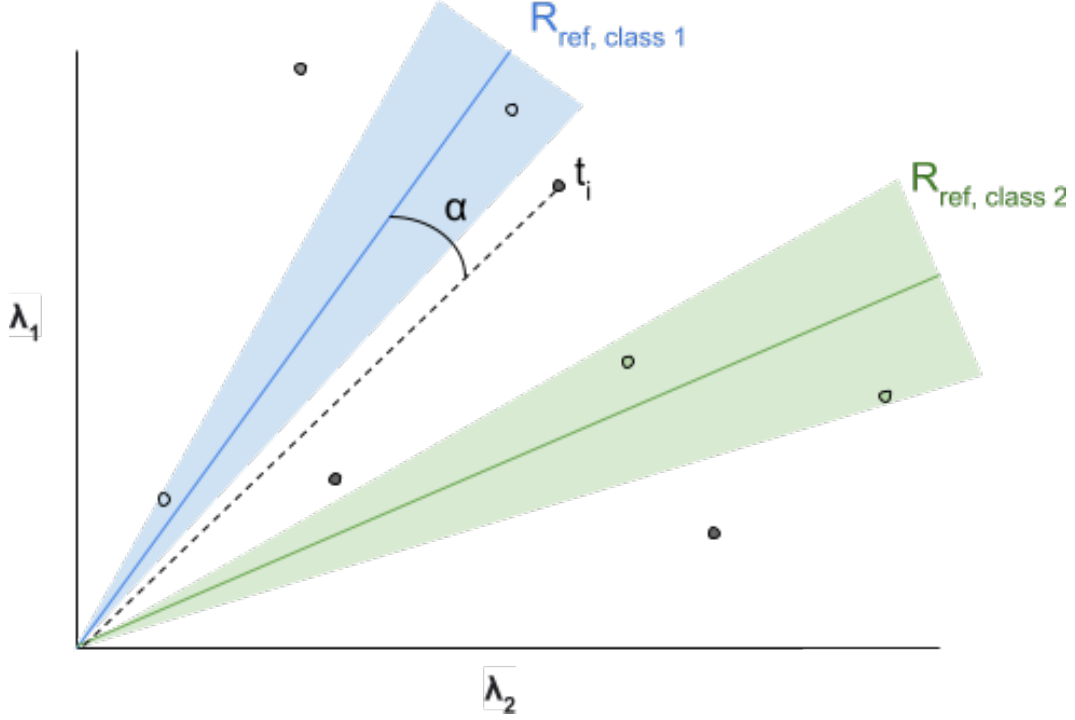


Figure 17. Visualisation of SAM, with two different reference spectra (green, blue) and their respective decision boundaries (shaded areas). The ‘test’ or ‘input’ pixel t_i value is given, with angle α relative to the reference spectrum.

557 Using (4) and (5), the SID score β is computed as follows:

$$\beta = \sum_{i=1}^C p_i * \log \frac{p_i}{q_i} + \sum_{i=1}^C q_i * \log \frac{q_i}{p_i} \quad (6)$$

558 A combination of the SID and SAM algorithms improves the robustness of spec-
 559 tral matching, which can yield significantly better classification compared to using SID
 560 or SAM separately (Du et al., 2004). In their paper, Du et al. (2004) showed that the
 561 combination of SID (β) and SAM (α) improved the detection and classification of sam-
 562 ple panels with different spectral signatures. They proposed and tested the SIDSAM score
 563 γ , calculated (7). In addition to using SID and SAM separately, the SIDSAM score is
 564 also applied to see whether it provides a more accurate classification of the hyperspec-
 565 tral images used in this study.

$$\gamma = \beta * \tan(\alpha) \quad (7)$$

566 Lastly, the calculation of the SAM score allows the establishment of decision bound-
 567 aries prior to classification. These are parameterised as the angle a given test pixel is al-
 568 lowed to diverge from the reference spectrum. Observations that do not fall within the
 569 decision boundaries of any reference spectrum are not classified.

570 References

- 571 Adão, T., Hruška, J., Pádua, L., Bessa, J., Peres, E., Morais, R., & Sousa, J. J.
 572 (2017). Hyperspectral imaging: A review on UAV-based sensors, data pro-
 573 cessing and applications for agriculture and forestry. *Remote Sensing*, 9(11),
 574 1110.
- 575 Al-Khafaji, S. L., Zhou, J., Zia, A., & Liew, A. W.-C. (2017). Spectral-spatial scale
 576 invariant feature transform for hyperspectral images. *IEEE Transactions on*
 577 *Image Processing*, 27(2), 837–850.
- 578 Balsi, M., Moroni, M., Chiarabini, V., & Tanda, G. (2021). High-Resolution Aerial
 579 Detection of Marine Plastic Litter by Hyperspectral Sensing. *Remote Sensing*,
 580 13(8), 1557.
- 581 Biermann, L., Clewley, D., Martinez-Vicente, V., & Topouzelis, K. (2020). Find-
 582 ing Plastic Patches in Coastal Waters using Optical Satellite Data. *Scientific*
 583 *Reports*, 10(1), 5364. Retrieved from [https://doi.org/10.1038/s41598-020-](https://doi.org/10.1038/s41598-020-62298-z)
 584 [62298-z](https://doi.org/10.1038/s41598-020-62298-z) doi: 10.1038/s41598-020-62298-z
- 585 Bonifazi, G., Capobianco, G., & Serranti, S. (2018). A hierarchical classifi-
 586 cation approach for recognition of low-density (LDPE) and high-density
 587 polyethylene (HDPE) in mixed plastic waste based on short-wave infrared
 588 (SWIR) hyperspectral imaging. *Spectrochimica Acta Part A: Molecular*
 589 *and Biomolecular Spectroscopy*, 198, 115–122. Retrieved from [http://](http://www.sciencedirect.com/science/article/pii/S1386142518301975)
 590 www.sciencedirect.com/science/article/pii/S1386142518301975 doi:
 591 <https://doi.org/10.1016/j.saa.2018.03.006>
- 592 Borrelle, S. B., Ringma, J., Law, K. L., Monnahan, C. C., Lebreton, L., McGivern,
 593 A., ... Hilleary, M. A. (2020). Predicted growth in plastic waste exceeds
 594 efforts to mitigate plastic pollution. *Science*, 369(6510), 1515–1518.
- 595 Borsoi, R. A., Imbiriba, T., Bermudez, J. C. M., Richard, C., Chanussot, J.,
 596 Drumetz, L., ... Jutten, C. (2020). Spectral variability in hyperspectral
 597 data unmixing: A comprehensive review. *arXiv preprint arXiv:2001.07307*.

- 598 Cardoso-Fernandes, J., Silva, J., Lima, A., Teodoro, A. C., Perrotta, M., Cauzid,
 599 J., & Roda-Robles, E. (2020). Characterization of lithium (Li) minerals from
 600 the Fregeneda-Almendra region through laboratory spectral measurements: a
 601 comparative study. In *Earth resources and environmental remote sensing/gis*
 602 *applications xi* (Vol. 11534, p. 115340N). International Society for Optics and
 603 Photonics.
- 604 Chang, C.-C., & Lin, C.-J. (2011). LIBSVM: a library for support vector machines.
 605 *ACM transactions on intelligent systems and technology (TIST)*, 2(3), 1–27.
- 606 Chein, I. C. (1999). Spectral information divergence for hyperspectral im-
 607 age analysis. In *Ieee 1999 international geoscience and remote sensing*
 608 *symposium. igarss'99 (cat. no.99ch36293)* (Vol. 1, pp. 509–511). doi:
 609 10.1109/IGARSS.1999.773549
- 610 Chein, I. C. (2000). An information-theoretic approach to spectral variability, simi-
 611 larity, and discrimination for hyperspectral image analysis. *IEEE Transactions*
 612 *on Information Theory*, 46(5), 1927–1932. doi: 10.1109/18.857802
- 613 Chen, Y., Zhu, L., Ghamisi, P., Jia, X., Li, G., & Tang, L. (2017). Hyperspectral im-
 614 ages classification with Gabor filtering and convolutional neural network. *IEEE*
 615 *Geoscience and Remote Sensing Letters*, 14(12), 2355–2359.
- 616 Cocking, J., Narayanaswamy, B. E., Waluda, C. M., & Williamson, B. J. (2022).
 617 Aerial detection of beached marine plastic using a novel, hyperspectral
 618 short-wave infrared (SWIR) camera. *ICES Journal of Marine Science*.
 619 Retrieved from <https://doi.org/10.1093/icesjms/fsac006> doi:
 620 10.1093/icesjms/fsac006
- 621 Corbari, L., Maltese, A., Capodici, F., Mangano, M. C., Sarà, G., & Ciralo, G.
 622 (2020). Indoor spectroradiometric characterization of plastic litters commonly
 623 polluting the Mediterranean Sea: toward the application of multispectral im-
 624 agery. *Scientific Reports*, 10(1), 1–12.
- 625 Danson, F. M., Steven, M. D., Malthus, T. J., & Clark, J. A. (1992). High-spectral
 626 resolution data for determining leaf water content. *International Journal of*
 627 *Remote Sensing*, 13(3), 461–470.
- 628 De Graaf, M. C. C., Van de Steeg, H. M., Voeselek, L., & Blom, C. (1990). *Vege-*
 629 *tatie in de uiterwaarden: de invloed van hydrologie, beheer en substraat*. KU.
- 630 Deka, P. C. (2014). Support vector machine applications in the field of hydrology: a

- 631 review. *Applied soft computing*, *19*, 372–386.
- 632 Du, Y., Chang, C.-I., Ren, H., Chang, C.-C., Jensen, J. O., & D’Amico, F. M.
633 (2004). New hyperspectral discrimination measure for spectral characteri-
634 zation. *Optical Engineering*, *43*(8), 1777–1786.
- 635 Garaba, S. P., Acuña-Ruz, T., & Mattar, C. B. (2020). Hyperspectral longwave
636 infrared reflectance spectra of naturally dried algae, anthropogenic plas-
637 tics, sands and shells. *Earth Syst. Sci. Data*, *12*(4), 2665–2678. Retrieved
638 from <https://essd.copernicus.org/articles/12/2665/2020/> doi:
639 10.5194/essd-12-2665-2020
- 640 Garaba, S. P., Aitken, J., Slat, B., Dierssen, H. M., Lebreton, L., Zielinski, O., &
641 Reisser, J. (2018). Sensing Ocean Plastics with an Airborne Hyperspectral
642 Shortwave Infrared Imager. *Environmental Science & Technology*, *52*(20),
643 11699–11707. Retrieved from <https://doi.org/10.1021/acs.est.8b02855>
644 doi: 10.1021/acs.est.8b02855
- 645 Garaba, S. P., Arias, M., Corradi, P., Harmel, T., de Vries, R., & Lebreton, L.
646 (2021). Concentration, anisotropic and apparent colour effects on optical
647 reflectance properties of virgin and ocean-harvested plastics. *Journal of Haz-
648 ardous Materials*, *406*, 124290.
- 649 Garaba, S. P., & Dierssen, H. M. (2020). Hyperspectral ultraviolet to shortwave
650 infrared characteristics of marine-harvested, washed-ashore and virgin plastics.
651 *Earth System Science Data*, *12*(1), 77–86.
- 652 Girouard, G., Bannari, A., El Harti, A., & Desrochers, A. (2004). Validated spectral
653 angle mapper algorithm for geological mapping: comparative study between
654 QuickBird and Landsat-TM. In *Xxth isprs congress, geo-imagery bridging
655 continents, istanbul, turkey* (pp. 12–23).
- 656 Goddijn-Murphy, L., & Dufaur, J. (2018). Proof of concept for a model of light
657 reflectance of plastics floating on natural waters. *Marine Pollution Bul-
658 letin*, *135*, 1145–1157. Retrieved from [http://www.sciencedirect.com/
659 science/article/pii/S0025326X18306088](http://www.sciencedirect.com/science/article/pii/S0025326X18306088) doi: [https://doi.org/10.1016/
660 j.marpolbul.2018.08.044](https://doi.org/10.1016/j.marpolbul.2018.08.044)
- 661 Gopinath, G., Sasidharan, N., & Surendran, U. (2020). Landuse classification of
662 hyperspectral data by spectral angle mapper and support vector machine in
663 humid tropical region of India. *Earth Science Informatics*, *13*(3), 633–640.

- 664 Hottel, H. C. (1976). A simple model for estimating the transmittance of direct
665 solar radiation through clear atmospheres. *Solar Energy*, 18(2), 129–134.
666 Retrieved from [https://www.sciencedirect.com/science/article/pii/](https://www.sciencedirect.com/science/article/pii/0038092X76900451)
667 0038092X76900451 doi: [https://doi.org/10.1016/0038-092X\(76\)90045-1](https://doi.org/10.1016/0038-092X(76)90045-1)
- 668 Huang, H., Qureshi, J. U., Liu, S., Sun, Z., Zhang, C., & Wang, H. (2021). Hyper-
669 spectral imaging as a potential online detection method of microplastics. *Bul-*
670 *letin of Environmental Contamination and Toxicology*, 107(4), 754–763.
- 671 Karlsson, T. M., Grahn, H., van Bavel, B., & Geladi, P. (2016). Hyperspectral imag-
672 ing and data analysis for detecting and determining plastic contamination in
673 seawater filtrates. *Journal of near infrared spectroscopy*, 24(2), 141–149.
- 674 Khaleghi, M., Ranjbar, H., Shahabpour, J., & Honarmand, M. (2014). Spectral
675 angle mapping, spectral information divergence, and principal component
676 analysis of the ASTER SWIR data for exploration of porphyry copper miner-
677 alization in the Sarduiyeh area, Kerman province, Iran. *Applied Geomatics*,
678 6(1), 49–58.
- 679 Knaeps, E., Sterckx, S., Strackx, G., Mijndonckx, J., Moshtaghi, M., Garaba,
680 S. P., & Meire, D. (2021). Hyperspectral-reflectance dataset of dry, wet and
681 submerged marine litter. *Earth System Science Data*, 13(2), 713–730.
- 682 Kruse, F. A., Lefkoff, A. B., Boardman, J. W., Heidebrecht, K. B., Shapiro, A. T.,
683 Barloon, P. J., & Goetz, A. F. H. (1993). The spectral image processing sys-
684 tem (SIPS)—interactive visualization and analysis of imaging spectrometer
685 data. *Remote sensing of environment*, 44(2-3), 145–163.
- 686 Kumar, P., Gupta, D. K., Mishra, V. N., & Prasad, R. (2015). Comparison of
687 support vector machine, artificial neural network, and spectral angle mapper
688 algorithms for crop classification using LISS IV data. *International Journal of*
689 *Remote Sensing*, 36(6), 1604–1617.
- 690 Lacis, A. A., & Hansen, J. (1974). A parameterization for the absorption of solar
691 radiation in the earth’s atmosphere. *Journal of Atmospheric Sciences*, 31(1),
692 118–133.
- 693 Li, X., Xiao, J., Fisher, J. B., & Baldocchi, D. D. (2021). ECOSTRESS estimates
694 gross primary production with fine spatial resolution for different times of day
695 from the International Space Station. *Remote sensing of environment*, 258,
696 112360.

- 697 Liu, Y., & Zheng, Y. F. (2005). One-against-all multi-class SVM classification using
698 reliability measures. In *Proceedings. 2005 IEEE International Joint Conference on*
699 *Neural Networks, 2005.* (Vol. 2, pp. 849–854). IEEE.
- 700 Martínez-Vicente, V., Clark, J. R., Corradi, P., Aliani, S., Arias, M., Bochow, M.,
701 ... Vethaak, A. D. (2019). Measuring Marine Plastic Debris from Space:
702 Initial Assessment of Observation Requirements. *Remote Sensing*, *11*(20). doi:
703 10.3390/rs11202443
- 704 Maximenko, N., Arvesen, J., Asner, G., Carlton, J., Castrence, M., Centurioni, L.,
705 ... Corradi, P. (2016). Remote sensing of marine debris to study dynamics,
706 balances and trends. *White Paper, Decadal Survey for Earth Science and*
707 *Applications from Space, 22.*
- 708 Mehrubeoglu, M., Van Sickle, A., & McLauchlan, L. (2020). Borrowing least squares
709 analysis from spectral unmixing to classify plastics in SWIR hyperspectral
710 images. In *Hyperspectral imaging and applications* (Vol. 11576, p. 115760B).
711 International Society for Optics and Photonics. doi: 10.1117/12.2584007
- 712 Meijer, L. J. J., van Emmerik, T., van der Ent, R., Schmidt, C., & Lebreton, L.
713 (2021). More than 1000 rivers account for 80% of global riverine plastic emis-
714 sions into the ocean. *Science Advances*, *7*(18), eaaz5803.
- 715 Moroni, M., & Mei, A. (2020). Characterization and Separation of Traditional and
716 Bio-Plastics by Hyperspectral Devices. *Applied Sciences*, *10*(8). doi: 10.3390/
717 app10082800
- 718 Moroni, M., Mei, A., Leonardi, A., Lupo, E., & Marca, F. L. (2015). PET and PVC
719 Separation with Hyperspectral Imagery. *Sensors*, *15*(1), 2205–2227. Retrieved
720 from <https://www.mdpi.com/1424-8220/15/1/2205>
- 721 Moshtaghi, M., Knaeps, E., Sterckx, S., Garaba, S., & Meire, D. (2021). Spectral
722 reflectance of marine macroplastics in the VNIR and SWIR measured in a
723 controlled environment. *Scientific Reports*, *11*(1), 1–12.
- 724 Murphy, R. J., Monteiro, S. T., & Schneider, S. (2012). Evaluating classification
725 techniques for mapping vertical geology using field-based hyperspectral sensors.
726 *IEEE Transactions on Geoscience and Remote Sensing*, *50*(8), 3066–3080.
- 727 Petropoulos, G. P., Vadrevu, K. P., Xanthopoulos, G., Karantounias, G., & Scholze,
728 M. (2010). A comparison of spectral angle mapper and artificial neural net-
729 work classifiers combined with Landsat TM imagery analysis for obtaining

- 730 burnt area mapping. *Sensors*, *10*(3), 1967–1985.
- 731 Reinders, H. J., & Land-Zandstra, A. M. (n.d.). Citizen Science voor Schone Riv-
732 ieren.
- 733 Ren, Z., Sun, L., & Zhai, Q. (2020). Improved k-means and spectral matching
734 for hyperspectral mineral mapping. *International Journal of Applied Earth
735 Observation and Geoinformation*, *91*, 102154. Retrieved from [https://
736 www.sciencedirect.com/science/article/pii/S0303243420300714](https://www.sciencedirect.com/science/article/pii/S0303243420300714) doi:
737 <https://doi.org/10.1016/j.jag.2020.102154>
- 738 Serranti, S., Palmieri, R., Bonifazi, G., & Cózar, A. (2018). Characterization of
739 microplastic litter from oceans by an innovative approach based on hyperspec-
740 tral imaging. *Waste Management*, *76*, 117–125. Retrieved from [https://
741 www.sciencedirect.com/science/article/pii/S0956053X18301466](https://www.sciencedirect.com/science/article/pii/S0956053X18301466) doi:
742 <https://doi.org/10.1016/j.wasman.2018.03.003>
- 743 Stuart, M. B., McGonigle, A. J. S., & Willmott, J. R. (2019). Hyperspectral Imag-
744 ing in Environmental Monitoring: A Review of Recent Developments and
745 Technological Advances in Compact Field Deployable Systems. *Sensors*,
746 *19*(14), 3071. Retrieved from [https://www.mdpi.com/1424-8220/19/14/
747 3071](https://www.mdpi.com/1424-8220/19/14/3071)
- 748 Tasserou, P., van Emmerik, T., Peller, J., Schreyers, L., & Biermann, L. (2021).
749 Advancing Floating Macroplastic Detection from Space Using Experimen-
750 tal Hyperspectral Imagery. *Remote Sensing*, *13*(12), 2335. Retrieved from
751 <https://www.mdpi.com/2072-4292/13/12/2335>
- 752 Themistocleous, K., Papoutsas, C., Michaelides, S., & Hadjimitsis, D. (2020). In-
753 vestigating Detection of Floating Plastic Litter from Space Using Sentinel-2
754 Imagery. *Remote Sensing*, *12*(16). doi: 10.3390/rs12162648
- 755 Van Belle, V., Pelckmans, K., Van Huffel, S., & Suykens, J. A. K. (2011). Improved
756 performance on high-dimensional survival data by application of Survival-
757 SVM. *Bioinformatics*, *27*(1), 87–94.
- 758 van Emmerik, T., & de Lange, S. (2022). *Pilot monitoring drijvend zwerfafval en
759 macroplastics in rivieren: jaarmeting 2021* (Tech. Rep.).
- 760 van Emmerik, T., Kieu-Le, T.-C., Loozen, M., van Oeveren, K., Strady, E., Bui, X.-
761 T., . . . Tassin, B. (2018). A Methodology to Characterize Riverine Macroplas-
762 tic Emission Into the Ocean. *Frontiers in Marine Science*, *5*(372). Retrieved

- 763 from <https://www.frontiersin.org/article/10.3389/fmars.2018.00372>
764 doi: 10.3389/fmars.2018.00372
- 765 van Emmerik, T., Roebroek, C. T. J., de Winter, W., Vriend, P., Boonstra, M., &
766 Hougee, M. (2020). Riverbank macrolitter in the Dutch Rhine-Meuse delta.
767 *Environmental Research Letters*.
- 768 van Lieshout, C., van Oeveren, K., van Emmerik, T., & Postma, E. (2020). Au-
769 tomated River Plastic Monitoring Using Deep Learning and Cameras. *Earth*
770 *and Space Science*, 7(8), e2019EA000960. Retrieved from [https://doi.org/](https://doi.org/10.1029/2019EA000960)
771 [10.1029/2019EA000960](https://doi.org/10.1029/2019EA000960) doi: 10.1029/2019EA000960
- 772 Wilcox, C. C., Montes, M., Yetzbacher, M., Edelberg, J., & Schlupf, J. (2018). An
773 ultra-compact hyperspectral imaging system for use with an unmanned aerial
774 vehicle with smartphone-sensor technology. In *Micro-and nanotechnology*
775 *sensors, systems, and applications x* (Vol. 10639, p. 1063919). International
776 Society for Optics and Photonics.
- 777 Wilkes, T. C., Pering, T. D., McGonigle, A. J. S., Tamburello, G., & Willmott, J. R.
778 (2017). A low-cost smartphone sensor-based UV camera for volcanic SO₂
779 emission measurements. *Remote Sensing*, 9(1), 27.
- 780 Ying, X. (2019). An overview of overfitting and its solutions. In *Journal of physics:*
781 *Conference series* (Vol. 1168, p. 22022). IOP Publishing.
- 782 Zheng, Y., Bai, J., Xu, J., Li, X., & Zhang, Y. (2018). A discrimination model
783 in waste plastics sorting using NIR hyperspectral imaging system. *Waste*
784 *Management*, 72, 87–98. Retrieved from [https://www.sciencedirect.com/](https://www.sciencedirect.com/science/article/pii/S0956053X17307602)
785 [science/article/pii/S0956053X17307602](https://www.sciencedirect.com/science/article/pii/S0956053X17307602) doi: [https://doi.org/10.1016/](https://doi.org/10.1016/j.wasman.2017.10.015)
786 [j.wasman.2017.10.015](https://doi.org/10.1016/j.wasman.2017.10.015)